coatings

MDPI

Article

Effect of Gradient Multilayer Design on Tribological Performance of TiN/TiSiN Coatings Prepared by Cathodic Arc Ion Plating

Rong Tu [1,2,3], Jiao Jiao [1,2], Mingquan Jiang [2], Mai Yang [2], Baifeng Ji [4,*], Tenghua Gao [5,*], Qizhong Li [2,6], Song Zhang [1,2] and Lianmeng Zhang [1,2]

1 Chaozhou Branch of Chemistry and Chemical Engineering Guangdong Laboratory, Chaozhou 521000, China
2 State Key Lab of Advanced Technology for Materials Synthesis and Processing, Wuhan University of Technology, Wuhan 430070, China
3 Advanced Engineering Technology Research Institute of Zhongshan City, Wuhan University of Technology, Xiangxing Road 6, Zhongshan 528400, China
4 School of Civil Engineering and Architecture, Wuhan University of Technology, Wuhan 430070, China
5 Department of Applied Physics and Physico-Informatics, Keio University, Yokohama 223-8522, Japan
6 Hubei Key Laboratory of Advanced Technology for Automotive Components, Wuhan University of Technology, Wuhan 430070, China
* Correspondence: jbfeng@whut.edu.cn (B.J.); gao@appi.keio.ac.jp (T.G.)

Abstract: Hard coatings, such as transition metal nitrides, have been widely applied to improve the mechanical properties and tribological performance of cutting tools. The coatings in various multilayered or gradient structures have been designed to meet the demands of more severe service environments and more precise processing requirements. In this work, TiN/TiSiN coatings in several gradient and multilayered structures were deposited on cemented carbides by cathodic arc ion plating using Ti and TiSi alloy targets. The modulation period (Λ) of the multilayer gradually varies with thickness, ranging from 6 to 46 nm. The gradient multilayer coatings consist of a nanocrystalline-amorphous composite with compact growth. The coating with a modulation period first increasing and then decreasing has the highest hardness of 38 GPa, and the maximum residual compressive stress of −2.71 GPa, as well as the minimum coefficient of friction (COF) and wear rate. Gradient and multilayer structures moderate the brittleness caused by the presence of amorphous SiNx phase and optimize the mechanical properties and tribological performances of the coatings.

Keywords: TiN/TiSiN coatings; gradient multilayer; cathodic arc ion plating; microstructure; mechanical properties

check for updates

Citation: Tu, R.; Jiao, J.; Jiang, M.; Yang, M.; Ji, B.; Gao, T.; Li, Q.; Zhang, S.; Zhang, L. Effect of Gradient Multilayer Design on Tribological Performance of TiN/TiSiN Coatings Prepared by Cathodic Arc Ion Plating. *Coatings* **2023**, *13*, 836. https://doi.org/10.3390/coatings13050836

Academic Editor: Philipp Vladimirovich Kiryukhantsev-Korneev

Received: 1 April 2023
Revised: 18 April 2023
Accepted: 24 April 2023
Published: 26 April 2023

1. Introduction

Hard coatings are an effective way to improve the mechanical properties and tribological performances of metal materials by increasing their surface hardness and wear resistance [1]. Titanium nitride (TiN) was the most common coating in the past [2] due to its high hardness, good adhesion to metals, and good tribological performance [3,4]. However, the TiN coating prepared by physical vapor deposition (PVD) typically exhibits a columnar-grained structure, which is unfavorable for its hardness [5,6]. Incorporation of Si in TiN coatings (TiSiN) is an effective way to improve the hardness [7] and high oxidation resistance [8] of the coatings because the amorphous SiN_x phase impedes the growth of columnar TiN grains. The presence of amorphous SiN_x phase can also increase the number of interfaces in the coatings, and these interfaces can act as barriers against crack diffusion [9]. TiSiN coatings tend to have high residual stresses under the action of high-energy ion bombardment during deposition processes [10,11]. However, highly residual stresses can affect the adhesive strength between the coating and the substrate of

monolithic TiSiN coatings [10]. Therefore, it is important to reduce the residual stress while maintaining the high hardness of the TiSiN coatings.

A multilayer coating is a coating formed by alternating the growth of different materials with a multilayer structure. By combining the advantages of each layer and designing the elements' composition and structure, a coating with excellent performance can be prepared to meet the severe requirements of modern manufacturing and processing. Layer thickness is an important factor affecting the performance of multilayer coatings. When the layer thickness is greater than 100 nm, dislocations tend to pile up at the interface, which follows the classical Hall–Petch effect [12]. When the layer thickness is less than 100 nm, the stress is not enough to make the dislocation pass through the interface, which follows the Orowan bowing mechanism [13,14]. The strengthening mechanism is mainly the dislocation confined layer slip (CLS) mechanism [15]. When the layer thickness is between 2 and 5 nm, the strengthening mechanism can be explained by the interface barrier strength (IBS) model [16]. The mechanical properties of the coating mainly depend on the interface strength, which is affected by the interlayer stress and the grain orientation [17].

Compared to monolayer coatings, gradient and multilayer coatings consisting of different transition nitride layers show superior mechanical strength due to their special interfaces [18]. It has been stated that the different stress characteristics and the alternating stress field formed by different sublayers can reduce the stress concentration and the overall stress [19–22]. Complex stress states affect crack propagation and deflection [23], thus influencing the hardness and elastic modulus of the coating. The nano-scale TiSiN/CrN multilayer [24] has an epitaxial growth structure and forms a coherent interface. The coating shows the super-hard effect under the influence of modulus-difference and an alternating stress field. However, the hardness and elastic modulus of the coating will decrease after the coherent interface is destroyed. In the TiSiN/TiN multilayer [25], the TiN ductile layer inserted into TiSiN can reduce the crack density, and the diffusion of TiN grains can also inhibit the growth of cracks, thereby reducing residual stress and improving the adhesive strength of the coatings. In TiSiN/TiAlN multilayer coatings [26], the modulation period increases from 18 nm to 170 nm, and the hardness and residual stress (34 GPa and −3.5 GPa) increases because of the increase of the thickness of the TiSiN sublayer. However, when the modulation period is 6 nm, the thickness and residual stress (38 GPa and −5.1 GPa) of the coating are significantly enhanced due to the decrease of the grain size and the formation of the superlattice structure. The modulation period of the multilayer coatings, i.e., the thickness of the repeated bi- or tri-layers, is a key factor that affects the coatings' properties [27]. A previous study by Wan et al. reported that the TiN/TiSiN coatings exhibit the highest hardness (about 34 GPa) with the modulation period of 22.5 nm [28]. Bartosik et al. revealed the correlation between the variations of the bilayer period and the residual strain in the TiAlN/TiSiN multilayer coating, implying that the minimum modulation period leads to the minimum in-plane compressive residual strains [29]. The gradient in the thickness and/or composition of each layer is effective to eliminate residual stresses as well as control the wear rate [30–33]. Chang et al. revealed that the multilayer coatings with transition layers showed a dense structure which improved the adhesion strength and high hardness, such as TiSiN/TiVN, CrAlSiN/TiVN, and AlCrSiN [18,33,34]. Cui et al. revealed that the TiN coatings with gradually increasing nano-grains had superior adhesion and tribology performances compared to the monolayer TiN coating [35]. At present, it is important to improve the quality and quantity of the interfaces, as well as the coherent strains, by designing the gradient structure and adjusting the modulation period of multilayer coatings to improve the mechanical properties and tribological performances.

In cathodic ion plating equipment, the substrates are rotated with respect to the different cathodic targets, which can spontaneously form a multilayer structure with interlayer interfaces at a constant rotation speed (R_s, rpm) [36]. The thickness of the sublayers was varied by adjusting R_s. In this study, TiN/TiSiN gradient multilayer coatings were deposited by cathodic arc ion plating using Ti and TiSi alloy targets based on different R_s and modulation periods (Λ, nm). The influence of multilayer and gradient structures

on the mechanical properties and tribological performances of TiN/TiSiN coatings were comprehensively investigated.

2. Experimental Details

2.1. Preparation and Characterization of TiN/TiSiN Coatings

The TiN/TiSiN gradient multilayer coatings were fabricated on Si (100) substrates, mirror-polished cemented carbide (WC −8% Co, Φ25 mm × 4 mm), and stainless steels (42 mm × 38 mm × 0.5 mm) by a multi-arc ion plating system (Guangdong Huicheng Vacuum Technology Co., Guangdong, China), with a Ti target (99.99% in purity, Φ124 mm × 16 mm) and a TiSi alloy target (75 to 25 in molar ratio of Ti to Si, Φ124 mm × 16 mm), as shown in the previous article [37]. The Ti and TiSi alloy targets were placed oppositely in a rectangular vacuum chamber. All the substrates were ultrasonically cleaned in alcohol for 15 min and placed on the substrate holder. Prior to deposition, the substrates were etched by Ar ion for 20 min at a pressure of 1.9 Pa and the negative bias of the substrate of 600~1000 V. During deposition, the working gas pressure of Ar and N_2 (99.99% in purity) atmosphere was kept at 1.3 Pa, and the deposition temperature was 350 °C. The substrate bias was fixed at −150 V, and the target currents of $Ti_{75}Si_{25}$ and Ti were 110 and 120 A, respectively. The distance between the target and the substrate was fixed at 240 mm. More details are shown in Table 1.

Table 1. Experimental parameters of TiN/TiSiN gradient multilayer coatings.

Parameter	Values
Target materials	Ti and $Ti_{75}Si_{25}$
Target current of Ti (A)	120
Target current of $Ti_{75}Si_{25}$ (A)	110
Operation pressure (Pa)	1.3
Deposition temperature (°C)	350
Nitrogen partial pressure (Pa)	0.9
Deposition time (min)	50
Bias voltage (V)	−150

The multilayer coatings with the fixed modulation period (Λ) were deposited at the constant rotating speed of the substrate holder within 1 to 6 rpm, marked as M1 to M6, respectively. Based on the above basic experimental conditions, the gradient structure in thickness of the multilayer coatings was modified by increasing or decreasing the rotation speed of the substrate holder (R_s) within 1 to 6 rpm, step by step, while the sublayer with the same thickness was formed at any constant R_s. The gradient structure was repeated for 1, 2, and 4 cycles for G1–G2, G3–G4, and G5–G6, respectively. The total deposition time was 50 min, including 2 min for the Ti metallic transition layer (about 100 nm) and 48 min for the TiN/TiSiN gradient multilayers, keeping almost the same thickness of the whole coatings. Details of the R_s and the deposition time are shown in Table 2.

Figure 1 shows the experimental details of specimens and the schematic diagrams of the TiN/TiSiN gradient multilayer coatings. The modulation period (Λ) in the G1~G6 gradient multilayer coatings varied with the increasing deposition time (Figure 1a). In Figure 1b, the different colors represent different layers, showing different rotation speeds within 1 to 6 rpm, and the modulation periods of the TiN/TiSiN bilayers with 6 to 46 nm per rotation, respectively. All the G1~G6 coatings had a total of 168 TiN/TiSiN bilayers, i.e., 6, 12, and 24 gradient layers for G1–G2, G3–G4, and G5–G6 multilayers, respectively. The ideal thickness of all the coatings was 2.156 μm, including a Ti transition layer of 100 nm.

Table 2. Deposition details of the TiN/TiSiN gradient multilayer coatings.

Specimens	Total Deposition Time (min)	Ti Layer Deposition Time (min)	Rotation Speed (R_s, rpm)	Deposition Time per R_s (min)
G1	50	2	Increasing from 1 to 6	8
G2	50	2	Decreasing from 6 to 1	8
G3	50	2	Decreasing from 6 to 1, then increasing to 6	4
G4	50	2	Increasing from 1 to 6, then decreasing to 1	4
G5	50	2	Decreasing–increasing–decreasing–increasing	2
G6	50	2	Increasing–decreasing–increasing–decreasing	2

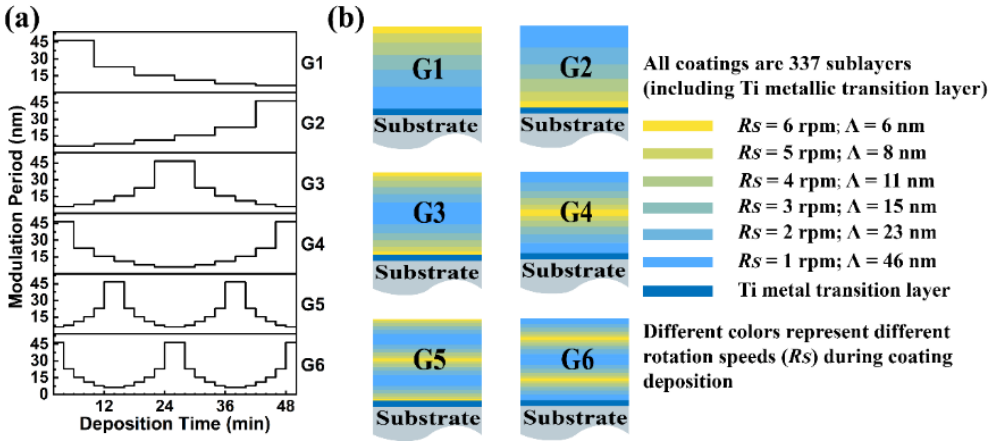

Figure 1. Schematic diagrams of (**a**) modulation period change with deposition time, (**b**) TiN/TiSiN coatings with gradient multilayer structures prepared at different R_s.

2.2. Microstructure and Component Tests

The phase structure was characterized by X-ray diffraction (XRD, D8 Advance from Bruker, Germany) using Cu Kα radiation. The chemical bonding structure was obtained by X-ray Photoelectron Spectroscopy (XPS, Thermo Scientific K-Alpha, Thermo Fisher Scientific, Waltham, MA, USA) using Al Kα radiation of 1486.6 eV. The cross-sectional and surface morphologies were observed by a Field Emission Scanning Electron Microscope system (FESEM, TESCAN MIRA LMS from TESCAN, Brno, Czech) equipped with an Energy-Dispersive Spectrometer (EDS, Aztec Energy). The nanostructures of the coatings were observed by transmission electron microscopy (TEM) and scanning transmission electron microscopy (STEM) using Talos F200S from TEM, Houston, TX, USA, operated at 200 kV.

2.3. Mechanical and Tribological Tests

The residual stresses were tested using X-ray diffraction (SmartLab, Rigaku Corporation, Tokyo, Japan) based on the $\sin^2\psi$ method using Cu radiation. Six incident angles were selected for each coating, and the residual stress was calculated by numerical fitting after the measurements. The hardness (H) and elastic modulus (E) of the coatings were tested by a nano-indentation instrument (T1-980, Bruker-Hysitron, Germany) equipped with a Berkovich diamond tip, with a load of 8 mN and an indentation depth of about 150 nm, less than 1/10 of the coating thickness. The adhesive strengths and the tribological properties were tested with a multi-functional surface tester (MFT-4000, Lanzhou Huahui Instrument Technology Co., Ltd., Lanzhou, China). The adhesive strength was tested by a scratch test. The indenter was continuously loaded from 0 to 100 N with a conical diamond tip of 0.2 mm radius, and a scratch length of 5 mm. Acoustic emission and frictional signals

were collected via sensors connected to the indenter. Ball-on-disc dry sliding tests were conducted using an Al_2O_3 ball of 5 mm in diameter as the counterpart at a normal load of 15 N, a reciprocating friction distance of 8 mm, a sliding speed of 200 mm/min, a sliding time of 3600 s, and a temperature of 25 °C. The depth and width of the worn surface were characterized by confocal laser scanning microscopy (LSM 800, Zeiss, Jena, Germany). The surface morphologies of wear tracks were observed using SEM and EDS.

3. Results and Discussion

3.1. Phase Composition and Microstructure

The XRD patterns of the TiN/TiSiN coatings with different gradient multilayer structures on stainless steel are shown in Figure 2. Face-centered cubic TiN were identified with a strong (111) preferential orientation. No crystalline SiN_x or titanium silicide peaks were observed, but the peaks of TiN shifted to higher angles, indicating that a compressive strain out-of-plane was applied [38]. This compressive strain is due to the strain misfit around the interface [39], indicating that Si formed a solid solution substituting for Ti atoms in the lattice and/or formed an amorphous SiN_x phase [40]. Figure 2 reveals a shift to a higher diffraction angle for the coatings on stainless steel compared to the standard peak positions for TiN (PDF#87-0631). Combined with HRTEM images, the lattice constant of the coating was 4.14 Å ± 0.02, which is smaller than the lattice constant of 4.24 Å of pure TiN reported in the literature. Therefore, residual compressive stress will be generated in the coating to cause the diffraction peak to shift to a high angle. This result is consistent with the XRD results. The crystallite sizes were calculated from the peak position of (111) in XRD according to the Scherrer's law [41]: $D = K\lambda/\beta\cos\theta$, in which D is the crystallite size, K is the Scherrer's constant of 0.89, λ is the wavelength of 0.154056 nm, β is FWHM, and θ is the diffraction angle. The crystallite sizes of the coatings were almost the same, i.e., 16.4, 15.9, 16.1, 16.0, 16.2, and 16.1 nm for G1 to G6, respectively.

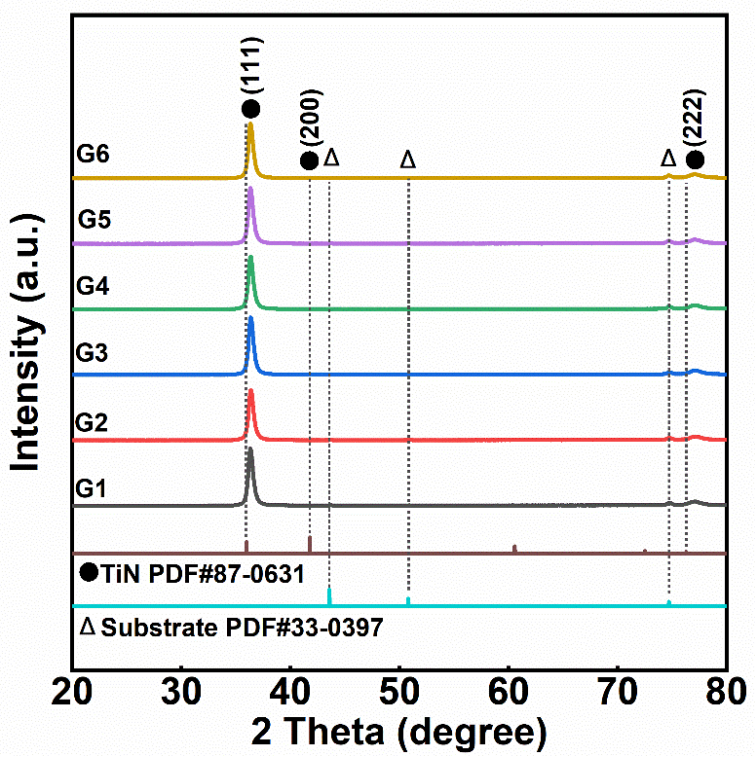

Figure 2. XRD patterns of TiN/TiSiN coatings with different gradient multilayer structures of G1~G6.

Elemental chemical states of the top coating were characterized by high-resolution spectra of XPS. The Ti 2p core-level spectra in Figure 3a reveals three groups of peaks at 455

and 461 eV, 456 and 462 eV, and 458.2 and 464 eV, corresponding to TiN [42], Ti_2O_3 [43], and TiO_2 [44], respectively. The peaks of TiO_2 and Ti_2O_3 are ascribed to the fact that titanium is easily oxidized by absorbing oxygen on the coating surface after exposing it to air [41]. Figure 3b shows the Si 2p peak at 101.8 eV, corresponding to SiN_x [45], indicating that the Si element formed mainly as the amorphous phase in the coatings. Figure 3c shows the N 1s spectra of Ti-N satellite, Ti-N, and a small amount of Si-N (SiN_x), with binding energies at 396.4, 397.1, and 399 eV, respectively. The relative strength ratio of Si-N (SiN_x) to Ti-N was consistent with the element ratio of Si to Ti [46].

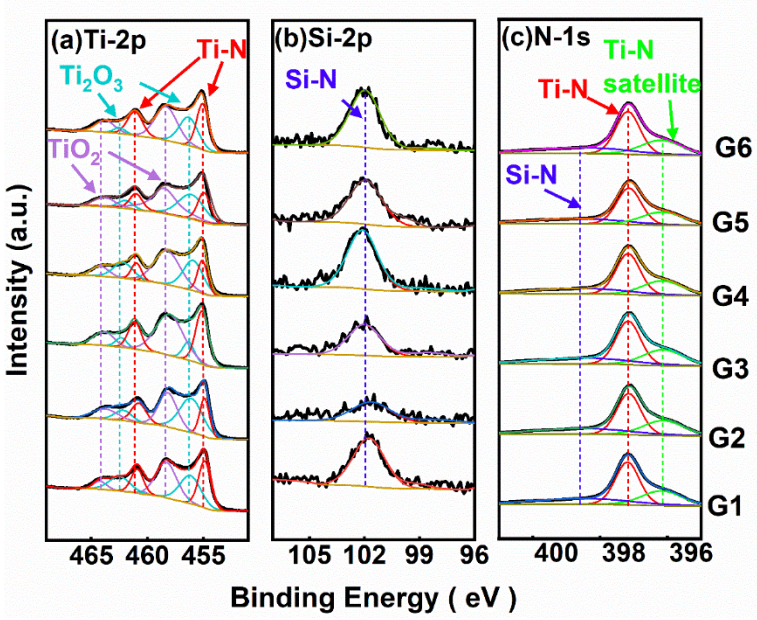

Figure 3. XPS spectra of Ti 2p (**a**), Si 2p (**b**), and N 1s (**c**) on the top layer of TiN/TiSiN coatings.

The cross-sectional micrographs of TiN/TiSiN gradient multilayer coatings are shown in Figure 4. The incorporation of Si inhibited the grain growth and induced grain re-nucleation [47], resulting in a dense and compact structure for all coatings. The thickness in this study was between 2.17 and 2.66 µm, indicating a deposition rate of 43.3 to 53.2 nm/min.

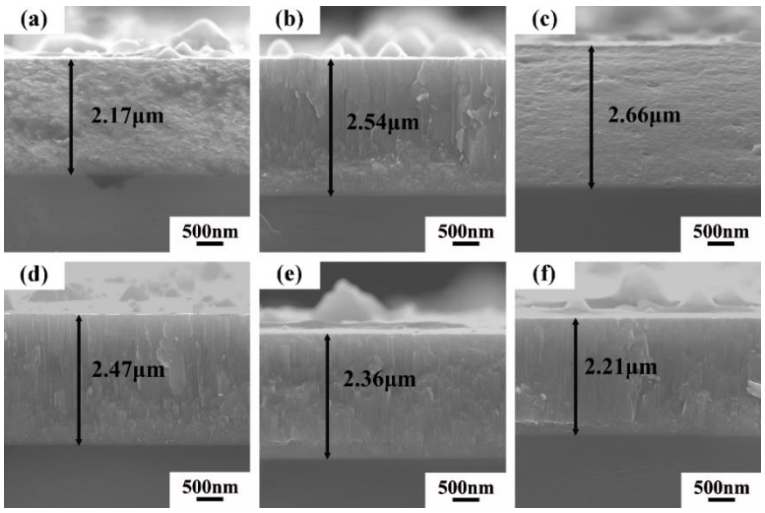

Figure 4. Cross-sectional SEM images of TiN/TiSiN multilayer coatings with different gradient structures of G1 (**a**), G2 (**b**), G3 (**c**), G4 (**d**), G5 (**e**), and G6 (**f**).

Figure 5a shows the cross-sectional TEM images of TiN/TiSiN coatings with the gradient multilayer structure of G1. Since the Si content in the coating was 4 at%, the TiSiN layer had a columnar microstructure, which was similar to that of the TiN layer. Since the modulation period of the TiN and TiSiN bilayer in the G1 gradient multilayer coating decreased with the deposition time, at the mid-term and later stage in Figure 5b,c, the modulation period decreased to 20 and 6 nm, where it was difficult to distinguish the layered structure. On the other hand, the locally enlarged images and mapping distribution of Si at the early growth stage, as shown in Figure 5d, corresponding to square d in Figure 5a, showed an obvious interface of the TiN and TiSiN layers. Figure 5e,f show HRTEM images of the TiN layer and the TiSiN layer in the G1 structural coating, corresponding to the areas (e) and (f) in Figure 5d. Si as amorphous SiN_x was distributed in the TiN martrix, in which the TiN nanocrystals were less than 10 nm in grain size. The fast Fourier transformation (FFT) in Figure 5 indicates that the layer exhibited an FCC structure with the TiN (111) preferred orientation. In addition, the surface energy in B1-NaCl was the lowest for (200) planes, so it might be assumed that processes of interrupted growth and re-nucleation led to the (200)-oriented growth [48]. The inverse FFT (IFFT) images corresponding to the areas 1 and 2 in Figure 5f show the *d*-value of 0.237 nm of TiN (111) grains in area 1, while the non-regular IFFT corresponding to area 2 indicates the boundary of the crystalline and amorphous phase [40]. The amorphous phase may prohibit the growth of TiN columnar grains. Figure 5g shows a dense, cross-sectional TEM image of the G3 structural coating, where no obvious columnar crystals from bottom to top penetration were seen, compared to the G1 structural coating. Figure 5h shows an HRTEM image of the TiSiN layer near the surface. The amorphous phase SiN_x was diffused in the TiSiN layer in an irregular shape. The IFFT image corresponding to square 3 in Figure 5h shows the *d*-value of 0.15 nm of TiN (220) grain, TiN (111) grain, and amorphous phase SiN_x. The grain boundaries are commonly considered as a weak spot for crack formation [23,49]. However, the interfaces formed between the nanocrystals and the amorphous phase SiN_x can prevent crack growth or expansion and grain boundary sliding, resulting in high hardness [50].

3.2. Mechanical Properties of Coatings

Nano-indentation tests were also employed to characterize the hardness (H) and elastic modulus (E) of TiN/TiSiN multilayer coatings at the fixed rotation speed. Figure 6 shows the modulation period (Λ) and mechanical properties of the TiN/TiSiN multilayer coatings under the same experimental conditions, except for rotation speed (R_s). The coating obtained the highest hardness 34 GPa at Λ = 11 nm (R_s = 4 rpm), and the high elastic modulus of 361 GPa at Λ = 11~23 nm (R_s = 2~4 rpm), respectively. In the literature, the optimized Λ of multilayer coatings generally ranges from 9 to 18 nm, such as TiAlN/CrAlN [51], TiBN/CrN [52], TiN/MoN [53], and CrAlN/VN [54]. Kim et al. reported that an optimized bilayer period can hinder the dislocation motion through the two layers [55]. The interface can also retard the dislocation motion, which increases the hardness. Therefore, initially, the hardness of the coating increases with the increasing R_s. A further increase of R_s leads to a decrease of the Λ and an increase of inter-diffusion, resulting in a decrease of the H [28]. In order to evaluate the elastic strain to failure capacity [56] and resistance to plastic deformation of the coating [57], the H/E^* and H^3/E^{*2} values were calculated (the effective modulus E^* was calculated by the equation $E^* = E/(1-\nu^2)$, and the ν is Poisson's ratio, ν = 0.3). The H/E^* of such nitride coatings is usually between 0.05 and 0.1 [58]. In this study, the highest H/E^* = 0.08 and H^3/E^{*2} = 0.25 GPa were obtained at Λ = 11 nm (R_s = 4 rpm), which are at an excellent level.

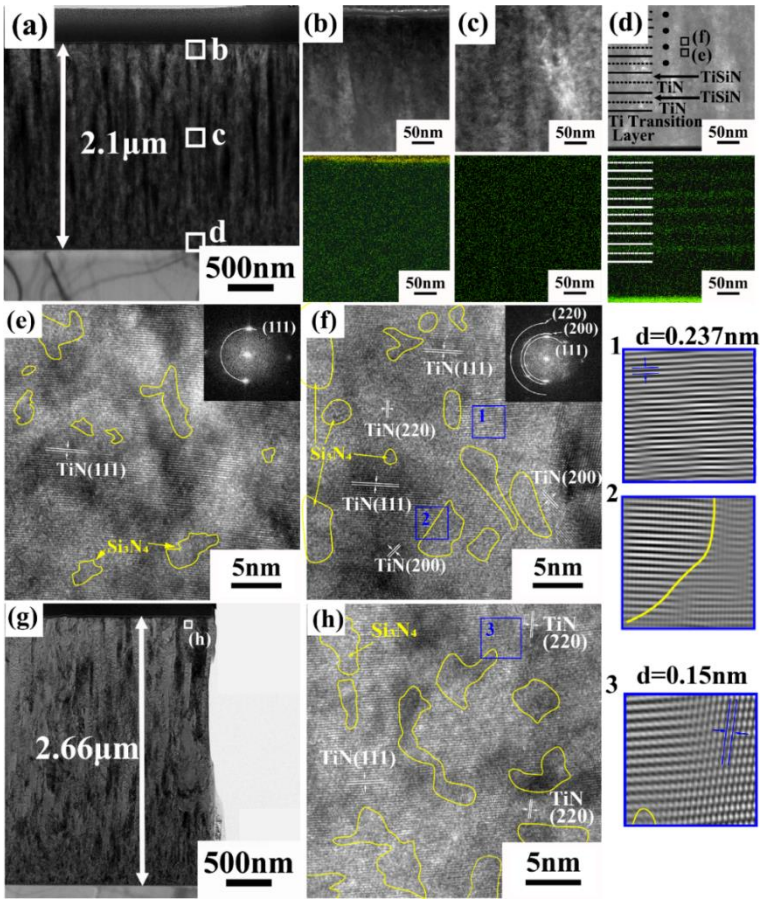

Figure 5. (**a**) Cross-sectional TEM image of TiN/TiSiN coating with the gradient multilayer structure of G1. (**b**–**d**) Local enlarged images and mapping distribution of Si corresponding to squares b, c, and d in (**a**). (**e**,**f**) HRTEM images of the TiN layer and the TiSiN layer of the G1 structural coating. Here, 1 and 2 are inverse fast Fourier transformation (IFFT) images corresponding to squares 1 and 2 in (**f**). (**g**) Cross-sectional TEM image of TiN/TiSiN coatings with the gradient multilayer structure of G3. (**h**) HRTEM image of the TiSiN layer near the surface. Here, 3 is the IFFT image corresponding to square 3 in (**h**).

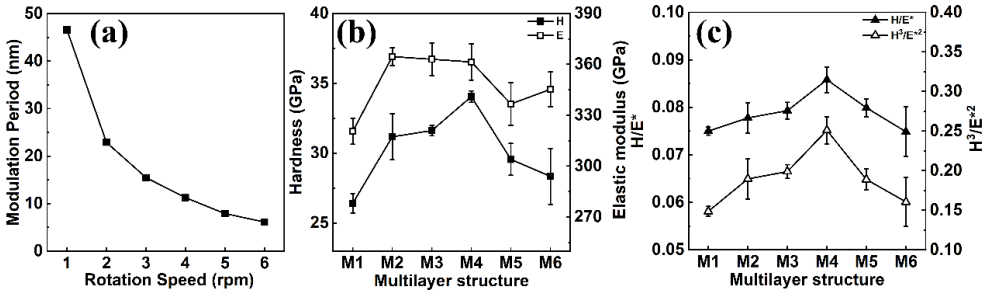

Figure 6. Modulation period of bilayer (**a**), nano-hardness and elastic modulus (**b**), and H/E* and H^3/E^{*2} ratios (**c**) of TiN/TiSiN coatings prepared at the fixed rotation speed.

Nano-indentation tests were also employed to characterize the mechanical properties of TiN/TiSiN gradient multilayer coatings. According to the nano-indentation test results of M1~M6 coatings, the H of the coatings first increased and then decreased with the decrease of the Λ. For the G1~G6 gradient multilayer coatings, the Λ gradually increased or decreased with the coating thickness, and the H and E of the corresponding sublayers also changed, which might have affected the results of nano-indentation. Figure 7a shows the loading–unloading curves. The indentation depth of less than 10% of the coating

thickness can eliminate the substrate effect as much as possible [59]. In this experiment, the maximum depths of indentations for all coatings were 102~120 nm, probably being influenced by the first, second, and third upper gradient layers for coatings G1–G2, G3–G4, and G5–G6, respectively. Figure 7b reveals that the elastic recovery ratio ranged from 47% to 57%, calculated by: $(h_{max} - h_f)/h_{max} \times 100\%$ (h_{max} stands for maximum penetration depth, h_f for contact depth). Under the action of load, irreversible plastic deformation took place in the coatings. Figure 7c shows the H and E of TiN/TiSiN multilayers with different gradient multilayer structures. The H of coatings varied from 32 to 38 GPa, while the E varied from 366 to 440 GPa. The E values of the coatings G1, G3, and G5 (small modulation period near the surface) were higher than those of G2, G4, and G6 (large modulation period near the surface). The H values of the coatings G3–G4 and G5–G6 showed the same trend, but the H value of the G1 structural coating was slightly smaller than the G2 structural coating. The highest H and E values were obtained simultaneously in the G3 structure. Figure 7d shows the ratios of the H/E^* and H^3/E^{*2}, which are usually applied to estimate the resistance ability to plastic deformation and the wear of the coatings, respectively. The G3 structural coating exhibited the highest H/E^* of 0.085 and the highest H^3/E^{*2} of 0.286 GPa.

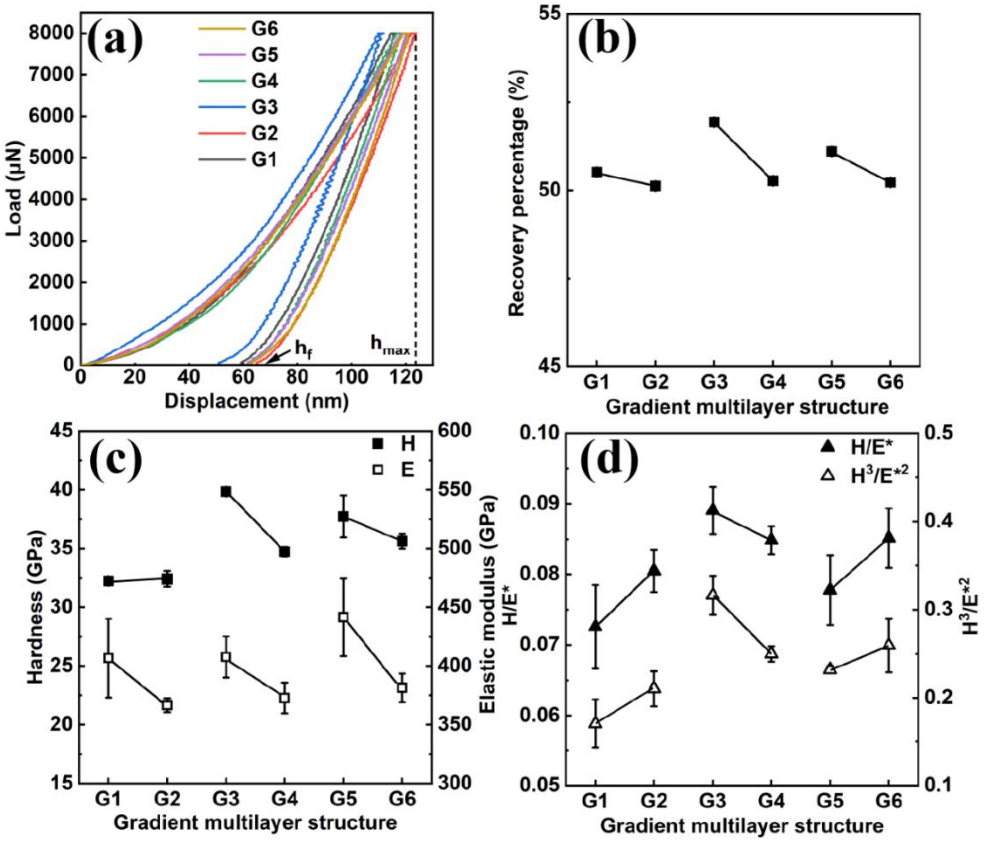

Figure 7. (**a**) Load–displacement curves for different structures, (**b**) corresponding to recovery percentage, (**c**) hardness and elastic modulus, and (**d**) H/E^* and H^3/E^{*2} ratios of gradient multilayer coatings.

The mechanical properties of the coatings are affected by the deposition method, elemental composition, and coating structures. To comprehensively assess the mechanical performance of the TiN/TiSiN gradient multilayer coatings, the relationships of H and E, and H/E^* and H^3/E^{*2} are presented in Figure 8. In [3,24,60–72], various MeSiN monolayer coatings containing Si and Me_1N/Me_2N (Me: Ti, Al, Cr, TiAl, etc.) multilayer coatings revealed excellent mechanical properties, e.g., the TiSiN/AlTiN coating had the highest H of 42 GPa and the E of 345 GPa, as well as the highest H/E^* and H^3/E^{*2} of 0.15 and 0.52 GPa, respectively. Moreover, the H and E of the coatings prepared by magnetron sputtering were lower than those prepared by cathodic arc ion plating. The H/E^* and H^3/E^{*2} of

multilayer coatings were slightly higher than those of monolayer coatings, indicating that multilayer coatings have a better ability to resist plastic deformation. In this work, the H and E of the TiN/TiSiN multilayer coatings (M1–M6) were significantly smaller than the gradient multilayer coatings (G3–G6), while the H/E* and H^3/E^{*2} were comparable to the G1, G2, and G5 coatings and smaller than the G3 structural coating. This indicates that most of the gradient multilayer structures had a significant effect on the hardness and elastic modulus of the coatings, and less so on the elastic strain to failure capacity and the resistance to plastic deformation of the coatings. The H and E of the TiN/TiSiN gradient multilayer coatings were located in the medial range, but the H/E* and H^3/E^{*2} ranked at an outstanding level, especially with both showing the highest values for the G3 structure, indicating that the toughness was simultaneously improved by the gradient multilayer.

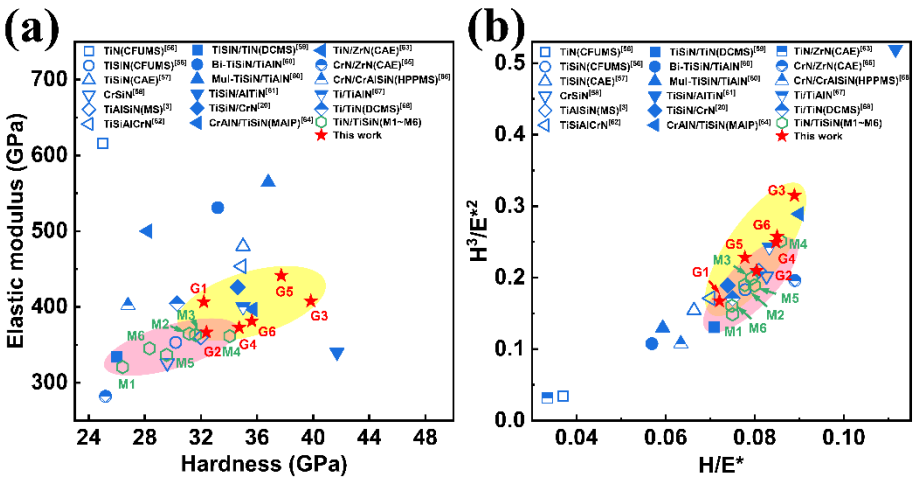

Figure 8. (**a**) The elastic modulus with respect to hardness and (**b**) H^3/E^{*2} ratios with respect to H/E* for the TiN/TiSiN gradient multilayer coatings, in comparison to the coatings containing Si in other references measured by nano-indentation [3,24,60–72].

XRD residual stress measurements were used to evaluate the macro-stress in the coatings, as shown in Figure 9. The compressive residual stresses of gradient multilayer coatings were −2.25, −2.71, −2.8, −1.9, −2.59, and −2.12 GPa, which are reduced in comparison to the monolayer TiSiN coating (about −7.8 GPa) [73], confirming that the construction of multilayer structures can effectively reduce the stresses [74]. Increasing the residual compressive stress can prevent the propagation of cracks and improve the resistance to adhesive wear of the coating, but excessive residual stress may cause the coating to separate from the substrate. The residual stress had a similar trend with the hardness, as shown in Figure 7c. It was reported that an appropriate compressive residual stress can decrease the friction coefficient and the wear rate, as well as reduce the adhesion aggregation [75]. Bobzin et al. reported that the compressive residual stress of the coating between −2 and −3 GPa may have the highest resistance to crack formation and the best cutting performance [76].

3.3. Tribological Properties

Figure 10 shows the coefficient of friction (COF) and the acoustic signal as a function of the scratching load. According to the change of the COF to determine the critical load of the coatings, L_{c2} is the critical load of the cohesive fracture of internal coatings, while L_{c3} is the spalling failure of the coatings [37]. With the increase of the load, the coatings showed some cracks and flakes slightly inside the scratch, and the width of the scratch gradually increased, accompanied by micro-spalling around the scratch, and the critical load is L_{c2}. Then, in the next stage, as the load increased, the micro-crack coalesced under a large shear stress, leading to the fracture of the coatings [64]. The L_{c2} values of different structural TiN/TiSiN coatings were between 44 and 57 N, and the L_{c3} values were between 56 and

66 N. The L_{c2} value was 57 N and the L_{c3} value was 66 N for the G3 structural coating, indicating a great improvement in adhesive strength. The G3 structural coating had the highest hardness and the largest residual stress, which improved the homogeneity of the coatings and led to stronger bonding [37].

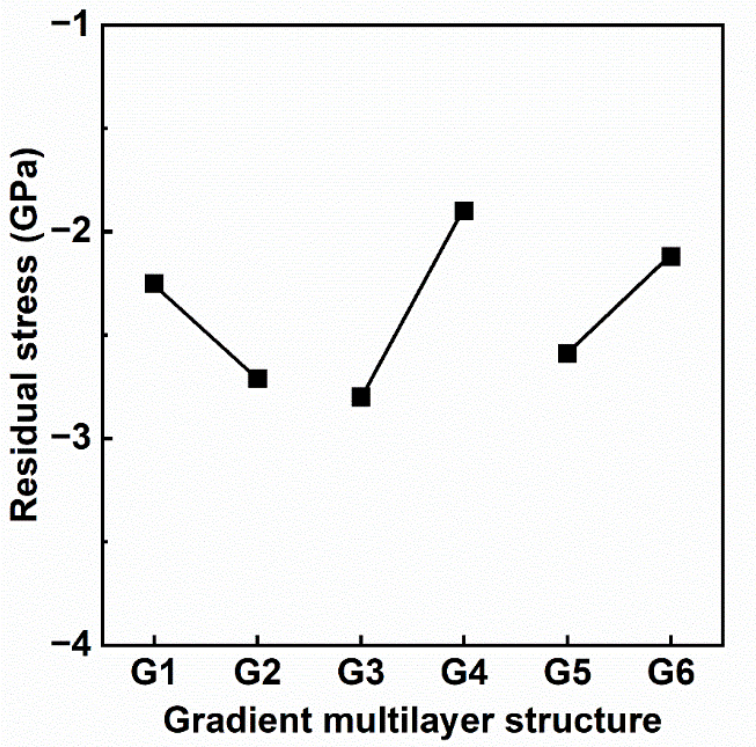

Figure 9. Residual compressive stress of TiN/TiSiN coatings with different gradient multilayer structures.

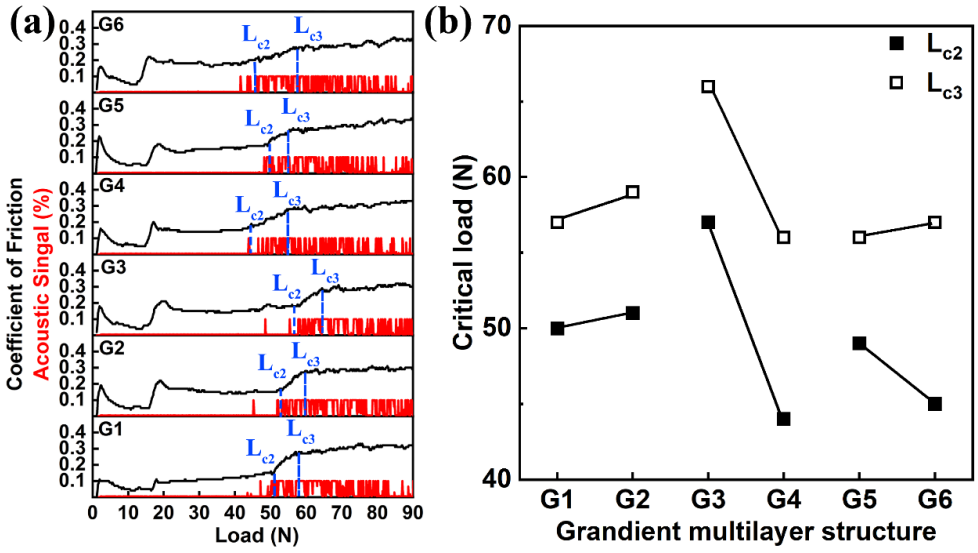

Figure 10. (**a**) COF and acoustic signal as a function of scratching load, and (**b**) L_{c2} and L_{c3} values of the TiN/TiSiN gradient multilayer coatings.

Figure 11 displays the three-dimensional topography and the SEM image of the local area of the G3 structural coating after the wear test. A slight furrow-like scratch was produced at the bottom of the wear scar of the G3 structural coating, accompanied by slight peeling (as shown in Figure 11a). During the reciprocating friction process of the sample, wear particles slid/rolled on the surface under the action of compressive and tangential

load. This motion led to the wear of the counterpart and scratches on the worn coating. The wear particles became smaller fragments and adhered to the coating surface. The plough action caused by a large amount of grinding debris made the coatings peel off [49]. The formation of abrasion grooves in the wear tracks was the dominant wear mechanism. According to Figure 11b, there was debris accumulation along both sides of the wear scar. Figure 11c shows SEM-EDS mappings, which confirmed that the peeled coating particles formed oxides, such as TiO_x.

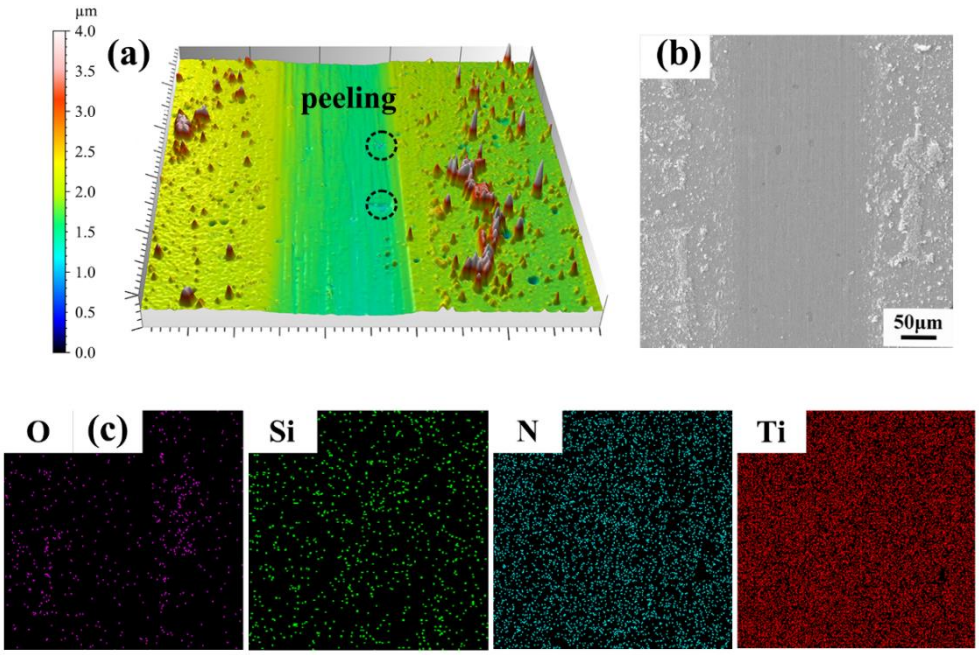

Figure 11. (**a**) Three-dimensional topography, (**b**) SEM image, and (**c**) EDS mappings of the worn surface of the G3 structural coating.

The evolution of the coefficient of friction (COF) along with the sliding distance for different multilayers at room temperature (RT) are depicted in Figure 12a. The COF increased in the initial running-in stage, and then reached a plateau during the steady-state friction period, and finally decreased after the friction time exceeded 45 min. Taking the G3 structural coating as an example, during the running-in stage, solid particles such as droplets on the coating surface first contacted with the Al_2O_3 counterpart, resulting in a sudden increase of the coefficient. Then, the solid particles were worn flat, the contact area became larger, and the COF decreased, entering the steady-state stage. When the friction time exceeded 45 min, along with the deepening of friction, the surface layer was removed, the particles falling off the coating were reduced, and the abrasive wear and the COF decreased. The COF was 0.5 to 0.6 for all gradient multilayer coatings, and the wear depth varied from 500 to 800 nm with the wear rate of 4.4×10^{-3}~6.1×10^{-3} mm^3 $(Nm)^{-1}$, as shown in Figure 12b,c. The presence of a thin friction layer comprising a lubricant phase such as titanium oxide may have contributed to the lower COF of the multilayer coatings compared to the TiSiN coating (the COF range of 0.7 to 1.1) [34,47,77]. The G3 structural coating had the minimum COF and the minimum wear rate of 4.4×10^{-3} $mm^3(Nm)^{-1}$. Generally, coatings with a higher hardness have a smaller COF. Therefore, the G3 structural coating, which had the highest H, showed the lowest COF. The H^3/E^{*2} ratio is correlated with the resistance to plastic deformation, which reveals the relative wear resistance [49], so the G3 structural coating had the smallest wear rate compared to the others, and had the highest H/E^* and H^3/E^{*2}.

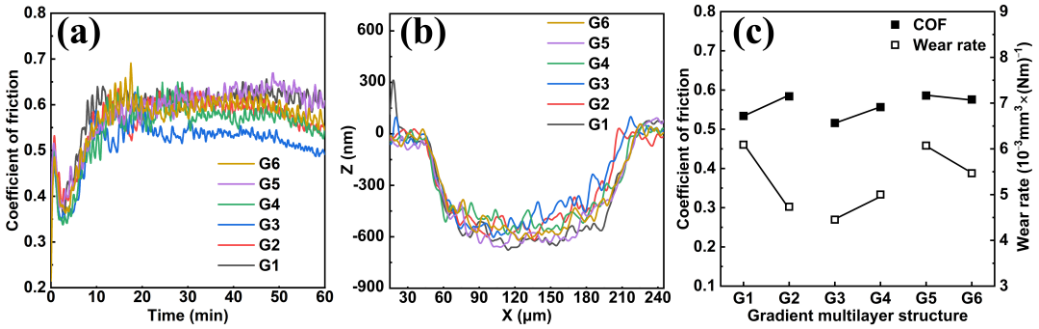

Figure 12. (**a**) Coefficient of friction curves of different coatings, (**b**) depth profile of the wear path of different coatings, and (**c**) the values of the coefficient of friction and the wear rate.

4. Conclusions

TiN/TiSiN gradient multilayer coatings were prepared using multi-arc ion plating. The coatings consisted of columnar nanocomposites by crystalline TiN phase and amorphous SiN_x phase, with a modulation period from 46 to 6 nm. Limited dislocation activity in nanocrystals and hindering of grain boundary sliding resulted in a high hardness of 32~38 GPa, showing the maximum H/E* and H^3/E^{*2} in the G3 gradient multilayer structure, with a modulation period of 6 and 8 nm, and within the top layers of about 300 nm in thickness. The wear behavior of the coatings was abrasive wear, accompanied by oxidation, showing the lowest COF (0.51) and wear rate (4.4×10^{-3} mm^3 (Nm)$^{-1}$), and the maximum critical load values (57 N for L_{c2} and 66 N for L_{c3}), which demonstrated the highest adhesive strength in the G3 structural coating, where the modulation period increased from 6 to 46 nm, and then decreased.

Author Contributions: Conceptualization, R.T., J.J., M.J., M.Y., B.J., T.G., Q.L., S.Z. and L.Z.; Data curation, R.T. and J.J.; Funding acquisition, Q.L.; Investigation, J.J.; Project administration, Q.L.; Resources, S.Z.; Supervision, R.T.; Writing—original draft, J.J.; Writing–review & editing, R.T. All authors have read and agreed to the published version of the manuscript.

Funding: This work was supported by the Guangdong Major Project of Basic and Applied Basic Research (2021B0301030001), the Self-Innovation Research Funding Project of Hanjiang Laboratory (HJL202012A002, HJL202012A003), and the Major Science and Technology Project in Zhongshan City, Guangdong Province (2019AG029). This work was also supported by the National Natural Science Foundation of China (Nos. 51861145306, 51872212, 51972244, 52002075, and 62204179), and the 111 Project (B13035). It was further supported by the International Science & Technology Cooperation Program of China (2018YFE0103600) and the Technological Innovation of Hubei Province (2019AAA030), China.

Conflicts of Interest: The authors declare no conflict of interest.

References

1. Bai, Y.; Guo, T.; Wang, J.; Gao, J.; Gao, K.; Pang, X. Stress-sensitive fatigue crack initiation mechanisms of coated titanium alloy. *Acta Mater.* **2021**, *217*, 9. [CrossRef]
2. Çam, A.S.; Ergüder, T.O.; Kaya, G.; Yıldız, F. Improvement of structural/tribological properties and milling performances of tungsten carbide cutting tools by bilayer TiAlN/TiSiN and monolayer AlCrSiN ceramic films. *Ceram. Int.* **2022**, *48*, 26342–26350. [CrossRef]
3. Tillmann, W.; Dildrop, M. Influence of Si content on mechanical and tribological properties of TiAlSiN PVD coatings at elevated temperatures. *Surf. Coat. Technol.* **2017**, *321*, 448–454. [CrossRef]
4. Huang, X.; Etsion, I.; Shao, T. Effects of elastic modulus mismatch between coating and substrate on the friction and wear properties of TiN and TiAlN coating systems. *Wear* **2015**, *338–339*, 54–61. [CrossRef]
5. Wo, P.C.; Zhao, X.L.; Munroe, P.R.; Zhou, Z.F.; Li, K.Y.; Habibi, D.; Xie, Z.H. Extremely hard, damage-tolerant ceramic coatings with functionally graded, periodically varying architecture. *Acta Mater.* **2013**, *61*, 193–204. [CrossRef]
6. Xie, Z.H.; Hoffman, M.; Munroe, P.; Bendavid, A.; Martin, P.J. Deformation mechanisms of TiN multilayer coatings alternated by ductile or stiff interlayers. *Acta Mater.* **2008**, *56*, 852–861. [CrossRef]

7. Vereschaka, A.; Milovich, F.; Andreev, N.; Sotova, C.; Alexandrov, I.; Muranov, A.; Mikhailov, M.; Tatarkanov, A. Investigation of the structure and phase composition of the microdroplets formed during the deposition of PVD coatings. *Surf. Coat. Technol.* **2022**, *441*, 128574. [CrossRef]
8. Liu, Z.R.; Pei, F.; Chen, L.; Mayrhofer, P.H. Effect of Si-addition on structure and thermal stability of Ti-Al-N coatings. *J. Alloys Compd.* **2022**, *917*, 165483. [CrossRef]
9. Diserens, M.; Patscheider, J.; Lévy, F. Mechanical properties and oxidation resistance of nanocomposite TiN–SiN_x physical-vapor-deposited thin films. *Surf. Coat. Technol.* **1999**, *120*, 158–165. [CrossRef]
10. Chen, Z.; Lou, M.; Geng, D.; Xu, Y.X.; Wang, Q.; Zheng, J.; Zhu, R.; Chen, Y.; Kim, K.H. Effect of the modulation geometry on mechanical and tribological properties of TiSiN/TiAlN nano-multilayer coatings. *Surf. Coat. Technol.* **2021**, *423*, 127586. [CrossRef]
11. Cheng, Y.H.; Browne, T.; Heckerman, B.; Gannon, P.; Jiang, J.C.; Meletis, E.I.; Bowman, C.; Gorokhovsky, V. Influence of Si content on the structure and internal stress of the nanocomposite TiSiN coatings deposited by large area filtered arc deposition. *J. Phys. D Appl. Phys.* **2009**, *42*, 125415. [CrossRef]
12. Anderson, P.M.; Li, C. Hall-Petch relations for multilayered materials. *Nanostructured Mater.* **1995**, *5*, 349–362. [CrossRef]
13. Jang, T.J.; Choi, W.S.; Kim, D.W.; Choi, G.; Jun, H.; Ferrari, A.; Kormann, F.; Choi, P.P.; Sohn, S.S. Shear band-driven precipitate dispersion for ultrastrong ductile medium-entropy alloys. *Nat. Commun.* **2021**, *12*, 4703. [CrossRef] [PubMed]
14. Szajewski, B.A.; Crone, J.C.; Knap, J. Analytic model for the Orowan dislocation-precipitate bypass mechanism. *Materialia* **2020**, *11*, 100671. [CrossRef]
15. Misra, A.; Hirth, J.P.; Hoagland, R.G. Length-scale-dependent deformation mechanisms in incoherent metallic multilayered composites. *Acta Mater.* **2005**, *53*, 4817–4824. [CrossRef]
16. Zhou, Q.; Huang, P.; Liu, M.; Wang, F.; Xu, K.; Lu, T. Grain and interface boundaries governed strengthening mechanisms in metallic multilayers. *J. Alloys Compd.* **2017**, *698*, 906–912. [CrossRef]
17. Yu, K.Y.; Liu, Y.; Rios, S.; Wang, H.; Zhang, X. Strengthening mechanisms of Ag/Ni immiscible multilayers with fcc/fcc interface. *Surf. Coat. Technol.* **2013**, *237*, 269–275. [CrossRef]
18. Chang, Y.-Y.; Chiu, W.-T.; Hung, J.-P. Mechanical properties and high temperature oxidation of CrAlSiN/TiVN hard coatings synthesized by cathodic arc evaporation. *Surf. Coat. Technol.* **2016**, *303*, 18–24. [CrossRef]
19. Wan, Q.; Yang, B.; Liu, H.D.; Chen, J.; Zhang, J. Microstructure and adhesion of MeN/TiSiN (Me=Ti, Cr, Zr, Mo, Nb_xAl_{1-x}) multilayered coatings deposited by cathodic arc ion plating. *Appl. Surf. Sci.* **2019**, *497*, 143602. [CrossRef]
20. Vereschaka, A.; Aksenenko, A.; Sitnikov, N.; Migranov, M.; Shevchenko, S.; Sotova, C.; Batako, A.; Andreev, N. Effect of adhesion and tribological properties of modified composite nano-structured multi-layer nitride coatings on WC-Co tools life. *Tribol. Int.* **2018**, *128*, 313–327. [CrossRef]
21. Kameneva, A.; Kichigin, V. Corrosion, wear, and friction behavior of a number of multilayer two-, three- and multicomponent nitride coatings on different substrates, depending on the phase and elemental composition gradient. *Appl. Surf. Sci.* **2019**, *489*, 165–174. [CrossRef]
22. Ali, R.; Sebastiani, M.; Bemporad, E. Influence of Ti–TiN multilayer PVD-coatings design on residual stresses and adhesion. *Mater. Des.* **2015**, *75*, 47–56. [CrossRef]
23. Ecker, W.; Keckes, J.; Krobath, M.; Zalesak, J.; Daniel, R.; Rosenthal, M.; Todt, J. Nanoscale evolution of stress concentrations and crack morphology in multilayered CrN coating during indentation: Experiment and simulation. *Mater. Des.* **2020**, *188*, 108478. [CrossRef]
24. Li, W.; Liu, P.; Zhu, X.; Zhang, K.; Ma, F.; Liu, X.; Chen, X.; He, D. Si content dependent microstructure and mechanical properties of CrN/TiSiN nanomultilayered films. *Mater. Sci. Eng. A* **2014**, *610*, 28–32. [CrossRef]
25. Wo, P.C.; Munroe, P.R.; Zhou, Z.F.; Li, K.Y.; Xie, Z.H. Effects of TiN sublayers on the response of TiSiN nanocomposite coatings to nanoidentation and scratching contacts. *Mater. Sci. Eng. A* **2010**, *527*, 4447–4457. [CrossRef]
26. Chang, C.-L.; Chen, W.-C.; Tsai, P.-C.; Ho, W.-Y.; Wang, D.-Y. Characteristics and performance of TiSiN/TiAlN multilayers coating synthesized by cathodic arc plasma evaporation. *Surf. Coat. Technol.* **2007**, *202*, 987–992. [CrossRef]
27. Li, W.; Liu, P.; Meng, J.; Zhang, K.; Ma, F.; Liu, X.; Chen, X.; He, D. Microstructure and mechanical property of TiSiN nanocomposite film with inserted CrAlN nanomultilayers. *Surf. Coat. Technol.* **2016**, *286*, 313–318. [CrossRef]
28. Wan, Q.; Yang, B.; Chen, Y.M.; Cai, Y.; Liu, Y.; Meng, L.; Gao, D.X. Effect of bilayer period on microstructure and mechanical properties of TiSiN/TiN coatings. *Materialia* **2018**, *3*, 260–264. [CrossRef]
29. Bartosik, M.; Arndt, M.; Rachbauer, R.; Krywka, C.; Koller, C.M.; Keckes, J.; Mayrhofer, P.H. Cross-sectional X-ray nano-diffraction and -reflectivity analysis of multilayered AlTiN–TiSiN thin films: Correlation between residual strain and bi-layer period. *Scr. Mater.* **2015**, *107*, 153–156. [CrossRef]
30. Uysal, M.U. Numerical Modeling of Functional Graded TiB Coating in Nanoindentation on Determination of Mechanical Properties. *Mater. Today Proc.* **2015**, *2*, 217–223. [CrossRef]
31. Rao, H.; Jayasekara, I.; Dutta, B.; Maurice, D. Segregation phenomena during deposition of functionally graded zirconia-based ceramics with Stellite 21 on a steel substrate. *Surf. Coat. Technol.* **2020**, *383*, 125270. [CrossRef]
32. Saleh, B.; Jiang, J.; Fathi, R.; Al-hababi, T.; Xu, Q.; Wang, L.; Song, D.; Ma, A. 30 Years of functionally graded materials: An overview of manufacturing methods, Applications and Future Challenges. *Compos. Part B Eng.* **2020**, *201*, 108376. [CrossRef]
33. Chang, Y.Y.; Amrutwar, S. Effect of Plasma Nitriding Pretreatment on the Mechanical Properties of AlCrSiN-Coated Tool Steels. *Materials* **2019**, *12*, 795. [CrossRef] [PubMed]

34. Chang, Y.-Y.; Chang, H.; Jhao, L.-J.; Chuang, C.-C. Tribological and mechanical properties of multilayered TiVN/TiSiN coatings synthesized by cathodic arc evaporation. *Surf. Coat. Technol.* **2018**, *350*, 1071–1079. [CrossRef]
35. Cui, W.; Qin, G.; Duan, J.; Wang, H. A graded nano-TiN coating on biomedical Ti alloy: Low friction coefficient, good bonding and biocompatibility. *Mater. Sci. Eng. C* **2017**, *71*, 520–528. [CrossRef]
36. Veprek, S.; Veprek-Heijman, M.J.G. Industrial applications of superhard nanocomposite coatings. *Surf. Coat. Technol.* **2008**, *202*, 5063–5073. [CrossRef]
37. Tu, R.; Yang, M.; Yuan, Y.; Min, R.; Li, Q.; Yang, M.; Ji, B.; Zhang, S. Sandwich Structure to Enhance the Mechanical and Electrochemical Performance of TaN/(Ta/Ti)/TiN Multilayer Films Prepared by Multi-Arc Ion Plating. *Coatings* **2022**, *12*, 694. [CrossRef]
38. Daghbouj, N.; Sen, H.S.; Callisti, M.; Vronka, M.; Karlik, M.; Duchoň, J.; Čech, J.; Havránek, V.; Polcar, T. Revealing nanoscale strain mechanisms in ion-irradiated multilayers. *Acta Mater.* **2022**, *229*, 117807. [CrossRef]
39. Daghbouj, N.; Sen, H.S.; Čížek, J.; Lorinčík, J.; Karlík, M.; Callisti, M.; Čech, J.; Havránek, V.; Li, B.; Krsjak, V.; et al. Characterizing heavy ions-irradiated Zr/Nb: Structure and mechanical properties. *Mater. Des.* **2022**, *219*, 110732. [CrossRef]
40. Moritz, Y.; Saringer, C.; Tkadletz, M.; Stark, A.; Schell, N.; Letofsky-Papst, I.; Czettl, C.; Pohler, M.; Schalk, N. Oxidation behavior of arc evaporated TiSiN coatings investigated by in-situ synchrotron X-ray diffraction and HR-STEM. *Surf. Coat. Technol.* **2020**, *404*, 126632. [CrossRef]
41. Dang, C.; Yao, Y.; Olugbade, T.; Li, J.; Wang, L. Effect of multi-interfacial structure on fracture resistance of composite TiSiN/Ag/TiSiN multilayer coating. *Thin Solid Films* **2018**, *653*, 107–112. [CrossRef]
42. Chourasia, A.R.; Chopra, D.R. X-ray photoelectron study of TiN/SiO_2 and Ti/Si interfaces. *Thin Solid Films* **1995**, *266*, 298–301. [CrossRef]
43. Gonbeau, D.; Guimon, C.; Pfister-Guillouzo, G.; Levasseur, A. XPS study of thin films of titanium oxysulfides. *Surf. Sci.* **1991**, *254*, 81–89. [CrossRef]
44. Dementjev, A.P.; Ivanova, O.P.; Vasilyev, L.A.; Naumkin, A.V.; Nemirovsky, D.M.; Shalaev, D.Y. Altered layer as sensitive initial chemical state indicator. *J. Vac. Sci. Technol. A* **1994**, *12*, 423–427. [CrossRef]
45. Veprek, S.; Niederhofer, A.; Moto, K.; Bolom, T.; Männling, H.D.; Nesladek, P.; Dollinger, G.; Bergmaier, A. Composition, nanostructure and origin of the ultrahardness. *Surf. Coat. Technol.* **2000**, *152*, 133–134.
46. Kimura, T.; Yoshida, R.; Azuma, K. Titanium Silicon Nitride Films With Low Silicon Content Deposited via Reactive High-Power Pulsed Sputtering Penning Discharge. *IEEE Trans. Plasma Sci.* **2021**, *49*, 53–60. [CrossRef]
47. Oliveira, J.C.; Fernandes, F.; Ferreira, F.; Cavaleiro, A. Tailoring the nanostructure of Ti–Si–N thin films by HiPIMS in deep oscillation magnetron sputtering (DOMS) mode. *Surf. Coat. Technol.* **2015**, *264*, 140–149. [CrossRef]
48. Miletić, A.; Panjan, P.; Škorić, B.; Čekada, M.; Dražič, G.; Kovač, J. Microstructure and mechanical properties of nanostructured Ti–Al–Si–N coatings deposited by magnetron sputtering. *Surf. Coat. Technol.* **2014**, *241*, 105–111. [CrossRef]
49. Ma, Y.; Yang, J.; Tian, X.; Gong, C.; Zheng, W.; He, Y.; Gao, Z. Microstructure, adhesion, mechanical and corrosion properties of TiN coatings deposited by high energy pulse-enhanced vacuum arc evaporation. *J. Adhes. Sci. Technol.* **2019**, *34*, 1040–1061. [CrossRef]
50. Zhu, L.-H.; Song, C.; Ni, W.-Y.; Liu, Y.-X. Effect of 10% Si addition on cathodic arc evaporated TiAlSiN coatings. *Trans. Nonferrous Met. Soc. China* **2016**, *26*, 1638–1646. [CrossRef]
51. Li, P.; Chen, L.; Wang, S.Q.; Yang, B.; Du, Y.; Li, J.; Wu, M.J. Microstructure, mechanical and thermal properties of TiAlN/CrAlN multilayer coatings. *Int. J. Refract. Met. Hard Mater.* **2013**, *40*, 51–57. [CrossRef]
52. Zhou, S.Y.; Yan, S.J.; Han, B.; Yang, B.; Lin, B.Z.; Zhang, Z.D.; Ai, Z.W.; Pelenovich, V.O.; Fu, D.J. Influence of modulation period and modulation ratio on structure and mechanical properties of TiBN/CrN coatings deposited by multi-arc ion plating. *Appl. Surf. Sci.* **2015**, *351*, 1116–1121. [CrossRef]
53. Gao, Z.C.; Buchinger, J.; Koutna, N.; Wojcik, T.; Hahn, R.; Mayrhofer, P.H. Ab initio supported development of TiN/MoN superlattice thin films with improved hardness and toughness. *Acta Mater.* **2022**, *231*, 117871. [CrossRef]
54. Wang, Y.; Lee, J.-W.; Duh, J.-G. Mechanical strengthening in self-lubricating CrAlN/VN multilayer coatings for improved high-temperature tribological characteristics. *Surf. Coat. Technol.* **2016**, *303*, 12–17. [CrossRef]
55. Kim, Y.J.; Byun, T.J.; Han, J.G. Bilayer period dependence of CrN/CrAlN nanoscale multilayer thin films. *Superlattices Microstruct.* **2009**, *45*, 73–79. [CrossRef]
56. Leyland, A.; Matthews, A. On the significance of the H/E ratio in wear control: A nanocomposite coating approach to optimised tribological behaviour. *Wear* **2000**, *246*, 1–11. [CrossRef]
57. Akhter, R.; Zhou, Z.; Xie, Z.; Munroe, P. Influence of substrate bias on the scratch, wear and indentation response of TiSiN nanocomposite coatings. *Surf. Coat. Technol.* **2021**, *425*, 127687. [CrossRef]
58. Musil, J. Hard nanocomposite coatings: Thermal stability, oxidation resistance and toughness. *Surf. Coat. Technol.* **2012**, *207*, 50–65. [CrossRef]
59. Tu, R.; Yuan, Y.; Yang, M.; Min, R.; Jiao, J.; Li, Q.; Yang, M.; Ji, B.; Zhang, S. Effect of Negative Bias of HiPIMS and AIP Hybrid Deposition on Microstructure, Mechanical and Anti-Corrosive Properties of Cr_2N/TiN Multilayer Coatings. *Coatings* **2022**, *122*, 845. [CrossRef]
60. Akhter, R.; Zhou, Z.; Xie, Z.; Munroe, P. TiN versus TiSiN coatings in indentation, scratch and wear setting. *Appl. Surf. Sci.* **2021**, *563*, 150356. [CrossRef]

61. M'Saoubi, R.; Johansson, M.P.; Andersson, J.M. Wear mechanisms of PVD-coated PCBN cutting tools. *Wear* **2013**, *302*, 1219–1229. [CrossRef]
62. Fu, Y.; Zhou, F.; Zhang, M. The enhancement of individual friction and corrosion properties of CrSiN coatings by Mo doping in seawater. *Surf. Coat. Technol.* **2022**, *432*, 128069. [CrossRef]
63. Fernandes, F.; Al-Rjoub, A.; Cavaleiro, D.; Polcar, T.; Cavaleiro, A. Room and High Temperature Tribological Performance of Multilayered TiSiN/TiN and TiSiN/TiN(Ag) Coatings Deposited by Sputtering. *Coatings* **2020**, *10*, 1191. [CrossRef]
64. Zha, X.; Wang, T.; Chen, F.; Wang, J.; Lin, L.; Lin, F.; Xie, H.; Jiang, F. Investigation the fatigue impact behavior and wear mechanisms of bilayer micro-structured and multilayer nano-structured coatings on cemented carbide tools in milling titanium alloy. *Int. J. Refract. Met. Hard Mater.* **2022**, *103*, 105738. [CrossRef]
65. Geng, D.; Zeng, R.; Wu, Z.; Wang, Q. An investigation on microstructure and milling performance of arc-evaporated TiSin/AlTiN film. *Thin Solid Film.* **2020**, *709*, 138243. [CrossRef]
66. Yuan, Y.; Qin, Z.; Yu, D.; Wang, C.; Sui, J.; Lin, H.; Wang, Q. Relationship of microstructure, mechanical properties and hardened steel cutting performance of TiSiN-based nanocomposite coated tool. *J. Manuf. Process.* **2017**, *28*, 399–409. [CrossRef]
67. Frank, F.; Kainz, C.; Tkadletz, M.; Czettl, C.; Pohler, M.; Schalk, N. Microstructural and micro-mechanical investigation of cathodic arc evaporated ZrN/TiN multilayer coatings with varying bilayer thickness. *Surf. Coat. Technol.* **2022**, *432*, 128070. [CrossRef]
68. Li, C.; Wang, L.; Shang, L.; Cao, X.; Zhang, G.; Yu, Y.; Li, W.; Zhang, S.; Hu, H. Mechanical and high-temperature tribological properties of CrAlN/TiSiN multilayer coating deposited by PVD. *Ceram. Int.* **2021**, *47*, 29285–29294. [CrossRef]
69. Huang, S.-H.; Chen, S.-F.; Kuo, Y.-C.; Wang, C.-J.; Lee, J.-W.; Chan, Y.-C.; Chen, H.-W.; Duh, J.-G.; Hsieh, T.-E. Mechanical and tribological properties evaluation of cathodic arc deposited CrN/ZrN multilayer coatings. *Surf. Coat. Technol.* **2011**, *206*, 1744–1752. [CrossRef]
70. Chang, C.-L.; Huang, C.-H.; Lin, C.-Y.; Yang, F.-C.; Tang, J.-F. Mechanical properties of amorphous and crystalline CrN/CrAlSiN multilayer coating fabricated using HPPMS. *Surf. Interfaces* **2022**, *31*, 102064. [CrossRef]
71. Vogli, E.; Tillmann, W.; Selvadurai-Lassl, U.; Fischer, G.; Herper, J. Influence of Ti/TiAlN-multilayer designs on their residual stresses and mechanical properties. *Appl. Surf. Sci.* **2011**, *257*, 8550–8557. [CrossRef]
72. Sheng, L.; Xiao, Y.; Jiao, C.; Du, B.; Li, Y.; Wu, Z.; Shao, L. Influence of layer number on microstructure, mechanical properties and wear behavior of the TiN/Ti multilayer coatings fabricated by high-power magnetron sputtering deposition. *J. Manuf. Process.* **2021**, *70*, 529–542. [CrossRef]
73. Yang, S.-M.; Chang, Y.-Y.; Lin, D.-Y.; Wang, D.-Y.; Wu, W. Mechanical and tribological properties of multilayered TiSiN/CrN coatings synthesized by a cathodic arc deposition process. *Surf. Coat. Technol.* **2008**, *202*, 2176–2181. [CrossRef]
74. Zhang, Y.; Yang, Y.; Ding, H.; Peng, Y.; Zhang, S.; Yu, L.; Zhang, P. Combining magnetic filtered cathodic arc deposition with ion beam sputtering to afford superhard TiSiN multilayer composite films with tunable microstructure and mechanical properties. *Vacuum* **2016**, *125*, 6–12. [CrossRef]
75. Wu, Z.; Zheng, G.; Yan, J.; Cheng, X.; Liu, H.; Yang, X. Effect of TiAlSiN coating residual stress on its sliding wear and cutting wear performance. *Int. J. Adv. Manuf. Technol.* **2022**, *123*, 3885–3900. [CrossRef]
76. Bobzin, K.; Brögelmann, T.; Maier, H.J.; Heidenblut, T.; Kahra, C.; Carlet, M. Influence of residual stresses in hard tool coatings on the cutting performance. *J. Manuf. Process.* **2021**, *69*, 340–350. [CrossRef]
77. Cheng, Y.H.; Browne, T.; Heckerman, B.; Meletis, E.I. Mechanical and tribological properties of nanocomposite TiSiN coatings. *Surf. Coat. Technol.* **2010**, *204*, 2123–2129. [CrossRef]